Fourier Monte Carlo simulation of crystalline membranes in the flat phase

2013 J. Phys.: Conf. Ser. 454 012032

(http://iopscience.iop.org/1742-6596/454/1/012032)

Fourier Monte Carlo simulation of crystalline membranes in the flat phase

Andreas Tröster

Vienna University of Technology, Wiedner Hauptstrasse 8-10/136, A-1040 Wien, Austria

E-mail: andreas.troester@tuwien.ac.at

Abstract. Stimulated by the recent interest in graphene, the elastic behavior of crystalline membranes continues to be under debate. In their flat phase, one observes scaling of the correlation functions of in-plane and out-of-plane deformations $\boldsymbol{u}(\boldsymbol{x})$ and $f(\boldsymbol{x})$ at long wavelengths with respect to a given reference plane governed by a single universal exponent η. The purpose of the present article is to explain the ideas and techniques underlying our Fourier Monte Carlo simulation approach to the numerical determination of η in much greater detail than was possible in a recent letter that is currently under review. Our simulations are based on an effective Hamiltonian first derived by Nelson and Peliti formulated exclusively in terms of the Fourier amplitudes $\tilde{f}(\boldsymbol{q})$ of the field $f(\boldsymbol{x})$, and we calculate the out-of-plane correlation function $\langle|\tilde{f}(\boldsymbol{q})|^2\rangle = \tilde{G}(\boldsymbol{q})$ and their related mean squared displacement $\langle(\Delta f)^2\rangle$. The key to the progress reported in this work is the observation that on tuning the Monte Carlo acceptance rates separately for each wave vector, we are able to eliminate critical slowing down and thus achieve unprecedented statistical accuracy. A finite size scaling analysis for $\langle(\Delta f)^2\rangle$ gives $\eta = 0.795(10)$. In the alternative approach, where we study the scaling of $\tilde{G}(\boldsymbol{q})$, we observe an unexpected anisotropic finite size effect at small wave vectors which hampers a similarly accurate numerical analysis.

1. Introduction

Membranes are two-dimensional surfaces embedded in three-dimensional space, and like their one-dimensional cousins, the linear polymers, their phase diagram is determined by the competition between energy loss and entropy gain accompanying the membrane's exploration of possible deformed configurations. Sophisticated theoretical and computational approaches have been developed to classify the resulting wealth of phases and determine their properties. A full survey of all the corresponding past achievements is well beyond the scope of this article and we may refer the novice reader to the excellent source [1] instead. Instead, we only choose to focus on those aspects of the statistical mechanics of membranes that are needed in order to understand the context of our present work.

In classifying the various phases of fluctuating phases, most pertinent theories aim at computing the analytic properties (i.e. decay length scales and/or scaling powers) of the out-of-plane deformations (OPDs) and the surface unit normals and their correlation functions, since the membrane in-plane deformations (IPDs) are usually harder to assess experimentally. As a matter of fact, the variety of possible conformational phases of membranes is much richer than that of polymers, and it is worth noting that the corresponding universality classes of asymptotic long wavelength conformations also depend crucially on microscopic structural features of the

membrane, in contrast to what one might naively expect from arguments based on the standard renormalization group (RG) folklore. The explanation of this seemingly paradoxical statement is that distinct microstructures support different types of elastic interactions, which may induce long-range effective interactions between the OPDs. For instance, a membrane may have the microscopic characteristics of a two-dimensional liquid, with breaking and recombining bonds between its molecules. Familiar examples of such liquid membranes from soft matter physics are lipid bilayers [2]. Such a liquid membrane has a non-vanishing bending rigidity, but exhibits no static resistivity to shear, and its energy can thus only depend on its shape. It turns out that if self-avoidance effects are ignored, in which case one technically speaks of a "phantom" membrane model, liquid membranes are predicted to be always in a rotationally invariant "crumpled" phase, i.e. the correlations of their unit normals decay exponentially on a scale given by the so-called de Gennes-Taupin persistence length [3]. If only short-range interactions were at work, spontaneous breaking of this continuous symmetry would be ruled out by the Mermin-Wagner-Hohenberg theorem [4]. However, in [5] it was noted that the presence of (effective) long-range interactions between the unit normals may stiffen the membrane, and a so-called crumpling transition to a low temperature "flat" phase, whose long wavelength undulations define a new nontrivial universality class, may take place. In crystalline membranes, which support a nonzero shear modulus μ, such long-range forces are supplied by the shear-mediated coupling of the the IPDs to the OPDs. This is the case that we will concentrate on below, graphene being the most prominent, but certainly not the only example (see, e.g., [6, 7]). Relaxing the requirement of a regular lattice structure to that of a microscopic network of at the given temperature thermally unbreakable bonds defines so-called tethered membranes. Biological cell walls, which consist of lipid bilayers interacting with a shear-resistant protein network, the so-called cytoskeleton, are certainly the most important example of this species [8]. Inclusion of anisotropy in the elastic energy of a membrane may lead to tubular phases which appear flat in one and crumpled in the other direction. At finite temperature, a crystalline membrane may also undergo a dislocation unbinding transition to an hexatic phase [9], in which, even though μ vanishes, a residual directional bond stiffness remains, leading to an algebraic instead of an exponential decay of the correlations between the unit normals in this so-called crinkled phase for a phantom membrane. At present, there is good evidence but, at least to the author's best knowledge, no rigorous proof that when passing from phantom to physical membranes by inclusion of an energy penalty enforcing self-avoidance, the crumpled phases become unstable while self-avoidance remains irrelevant (in the RG sense) within the flat phases [10].

2. Theory

In the present work, we consider a continuum elastic energy model for an isotropic crystalline phantom membrane. In the Monge parameterization of the flat phase, membrane deformations with respect to a given two-dimensional reference plane with coordinates $\boldsymbol{x} = (x_1, x_2)$ are parameterized by a deformation vector field $(\boldsymbol{u}(\boldsymbol{x}), f(\boldsymbol{x}))$, where $\boldsymbol{u}$ is a two-dimensional vector of IPDs, while the "height function" f parameterizes the OPDs. As the membrane free energy is invariant under homogeneous translations, it can depend on deformations only via deformation gradients. Following [11, 12], an effective Hamiltonian containing all relevant couplings for describing the flat phase is given by

$$\tilde{\mathcal{H}}[f, \boldsymbol{u}] = \tilde{\mathcal{H}}_b[f] + \tilde{\mathcal{H}}_s[f, \boldsymbol{u}] \tag{1}$$

where the bending energy

$$\tilde{\mathcal{H}}_b[f] = \frac{\kappa_0}{2} \int d^2x \, (\Delta f)^2 \, (\boldsymbol{x}) \tag{2}$$

is augmented by an harmonic stretching part

$$\tilde{\mathcal{H}}_s[f,\boldsymbol{u}] = \frac{1}{2}\sum_{ij}\int d^2x\left(2\mu_0 u_{ij}^2(\boldsymbol{x}) + \lambda_0 u_{ii}(\boldsymbol{x})u_{jj}(\boldsymbol{x})\right) \tag{3}$$

Here κ_0 denotes the (bare) bending rigidity, $\Delta = \frac{\partial^2}{\partial x_1} + \frac{\partial^2}{\partial x_2}$ is the two-dimensional Laplacian and λ_0 and μ_0 are the bare Lamé constants. Moreover, in the Lagrangian strain tensor

$$u_{ij}(\boldsymbol{x}) = \epsilon_{ij}(\boldsymbol{x}) + f_{ij}(\boldsymbol{x}) \tag{4}$$

all nonlinear terms beyond the infinitesimal strain tensor

$$\epsilon_{ij}(\boldsymbol{x}) = \frac{1}{2}\left(\frac{\partial u_i(\boldsymbol{x})}{\partial x_j} + \frac{\partial u_j(\boldsymbol{x})}{\partial x_i}\right) \tag{5}$$

can be dropped for the IPDs, while one needs to keep a quadratic term symmetric "tensor potential"

$$f_{ij}(\boldsymbol{x}) = \frac{1}{2}\frac{\partial f(\boldsymbol{x})}{\partial x_i}\frac{\partial f(\boldsymbol{x})}{\partial x_j} \tag{6}$$

in the OPDs. In the continuum formalism presented in [12], which we sketch here for completeness, a transverse projector$P_{ij}^T = \delta_{ij} - \partial_i\partial_j/\Delta$ is employed to split $f_{ij}(\boldsymbol{x})$ into longitudinal and transverse parts $f_{ij}^L(\boldsymbol{x})$ and $f_{ij}^T(\boldsymbol{x})$, respectively. In the calculation of the partition function, the fact that $\epsilon_{ij}(\boldsymbol{x})$ is purely longitudinal allows $f_{ij}^L(\boldsymbol{x})$ to be "gauged away", i.e. absorbed into redefined path integration variables $\epsilon_{ij}(\boldsymbol{x}) \to \epsilon'_{ij}(\boldsymbol{x})$. Gaussian integration over these shifted variables produces a mere scalar factor, leaving a new effective Hamiltonian [11]

$$\mathcal{H}[f] = \frac{\kappa_0}{2}\int d^2x\,(\Delta f)^2 + \frac{K_0}{2}\int d^2x\left[P_{ij}^T f_{ij}(\boldsymbol{x})\right]^2 \tag{7}$$

for the OPDs which only involves the remaining transverse part $f_{ij}^T(\boldsymbol{x})$, where

$$K_0 = \frac{4\mu(\mu_0+\lambda_0)}{2\mu_0+\lambda_0} \tag{8}$$

is the bare 2d Young modulus [13]. This Hamiltonian resembles a field theory with a non-standard $\boldsymbol{q}^4$ type of dispersion, and a non-local fourth order contribution that, as promised above, resembles the effective long-range interaction of OPD's mediated by the eliminated IPD's. We introduce the continuous Fourier amplitudes

$$f(\boldsymbol{x}) = \int\limits_{|\boldsymbol{q}|>(2\pi/L)}^{|\boldsymbol{q}|<\Lambda} \frac{d^2q}{(2\pi)^2}\widehat{f}(\boldsymbol{q})e^{i\boldsymbol{q}\boldsymbol{x}} \tag{9}$$

where $\Lambda^{-1} \sim a$ denotes some microscopic length for which the continuum approximation ceases to be valid, and consider the correlations

$$\widehat{G}(\boldsymbol{p})\delta^2(\boldsymbol{p}+\boldsymbol{q}) \equiv \langle\widehat{f}(\boldsymbol{p})\widehat{f}(\boldsymbol{q})\rangle \tag{10}$$

of the OPD's. For a fluid membrane, μ_0 vanishes identically, which implies that $K_0 \equiv 0$ vanishes as well and the equipartition theorem applied to the remaining harmonic bending contribution yields

$$\widehat{G}(\boldsymbol{q}) = \frac{1}{\kappa_0 q^4} \tag{11}$$

In the case of a solid membrane it is tempting to try to do the same, i.e. ignore the term $\propto K_0$ as a first guess, which effectively amounts to a harmonic approximation. However, such a strategy fails to capture the essential physics of crystalline membrane elasticity, which, as we have stressed above, is caused by the effective long-range interaction encoded in the anharmonic part of (7). Technically, the coupling K_0 is relevant in the sense of the renormalization group and effectively leads to a renormalization of the bare bending rigidity κ_0. More precisely, one can show that the resulting renormalized bending rigidity acquires a nontrivial $\boldsymbol{q}$-dependence, such that actually

$$\widehat{G}(\boldsymbol{q}) = \frac{1}{\kappa(\boldsymbol{q}) q^4} \tag{12}$$

At this stage the critical exponent η is introduced as

$$\kappa(\boldsymbol{q}) \sim q^{-\eta} \tag{13}$$

The exponent η is indeed the central quantity governing the elastic behavior of the flat phase at long wavelengths, as other observables of interest like the $\boldsymbol{q}$-dependent scaling of the Lamé coefficients, the mean square height fluctuations (see below) and the correlation function of the unit normals are governed by scaling laws, whose critical exponents are related to η by simple algebraic scaling relations [13].

Due to the complicated structure of the anharmonic nonlocal fourth order term in (7), it is difficult to obtain precise estimates of η. Thus, the literature exhibits a remarkable dispersion of published numerical results for η, which are summarized in [8, 14]. Specifically, an early one-loop perturbative calculation by Nelson and Peliti [11] gave $\eta = 1$, whereas Le Doussal and Radzihovsky [15] obtained $\eta = 4/(1+\sqrt{15}) \approx 0.821$ from self-consistent RPA. RG calculations based on an ϵ-expansion [16] and a large-d expansion [17] have been carries out, but their numerical extrapolation to the physically relevant case of a two-dimensional membrane in three-dimensional space is not straightforward. Recently, the result $\eta = 0.849$ was derived from a nonperturbative RG approach [18]. Due to the difficulties encountered in these analytical approaches, extensive simulations have also been carried out. For instance, in [19] large-scale Monte Carlo simulations were performed based on a simple model with Gaussian spring pair potentials, and the estimates $\eta = 0.750(5)$ and $\eta = 0.72(4)$ were obtained from monitoring the mean squared fluctuations of IP and OP phonons (see below) and making use of the appropriate scaling relations. Motivated by the enormous interest in the properties of graphene, the problem was recently re-investigated with atomistic MC and molecular dynamics simulations based on a realistic many-body potential for carbon. While preliminary [20] conclusions based on the analysis of the observed normal-normal correlation function $\widehat{G}(\boldsymbol{q})$ of graphene membranes, which seemed to indicate a completely unexpected "preferred wavelength" for elastic fluctuations in graphene turned out to be based on artifacts caused by lack of sufficient convergence, subsequent work [21] bases on a simple pseudo-harmonic model finally yielded a result $\eta \approx 0.85$ in reasonable agreement with the bulk of the existing literature. These simulations are also very instructive, because, as is explained at length in the authoritative reference [13], they illustrate the crossover of $\widehat{G}(\boldsymbol{q})$ from mean-field (MF) ($\sim q^{-4}$) to critical ($\sim q^{-4+\eta}$) behavior, which roughly sets in at

a "Ginzburg wave vector"

$$q_G \approx \sqrt{\frac{3k_BTK_0}{8\pi\kappa_0^2}} \tag{14}$$

analytically defined by the breakdown of the harmonic approximation $K_0 \approx 0$ to the effective Hamiltonian (7). For graphene, using the parameters $T = 300\text{K}$, $K_0 = 12.4\mathring{A}^{-1}$ and $\kappa_0 = 1.1\text{eV}$ yields $q_G \approx 0.18\mathring{A}^{-1}$ [22, 23]. The relevance of such simulations for determining critical behavior depends, of course, on how far we are able to penetrate the scaling region. Obviously, a convenient measure for this ability is thus the ratio $q_G/(2\pi/L)$ of q_G to the smallest accessible wave vector component $2\pi/L$. Unfortunately, for the large scale atomistic MC simulations presented in [21] this ratio turns out to be only approximately 9. In other words, in each linear direction there are only 9 data points that may carry relevant information on the scaling region. For the purpose of determining η with sufficient precision it is clearly desirable to generate a larger fraction of relevant data.

3. Simulation

Common sense indicates that it may not be extremely efficient to base simulations of universal properties on atomistic potential models anyway. In calculating long wavelength characteristics, one should get rid of all irrelevant microscopic details that only make simulations more expensive, ideally ending up with an effective Hamiltonian like (7), which also allows to choose the coupling parameters κ_0, K_0 independently in a convenient way. Unfortunately, as mentioned above, the presence of the projector P_{ij}^T in (7) makes the fourth order contribution to (7) nonlocal, reflecting the long-range effective interaction of the OPD's induced by the IPD's. Thus, an attempt to base a real-space MC simulation directly on it is a rather hopeless enterprise. To clarify its nonlocal structure, let us rewrite (7) in terms of the Fourier amplitudes (9). Abbreviating $\hat{\boldsymbol{Q}} := \boldsymbol{Q}/|\boldsymbol{Q}|$, one finds [13]

$$\mathcal{H}_\Lambda[f] = \frac{\kappa_\Lambda}{2}\int \frac{d^2q}{(2\pi)^2} q^4 |\widehat{f}(\boldsymbol{q})|^2 + \frac{K_\Lambda}{8}\int \frac{d^2Q}{(2\pi)^2}|\widehat{\mathcal{F}}(\boldsymbol{Q})|^2 \tag{15}$$

where

$$\widehat{\mathcal{F}}(\boldsymbol{Q}) := \int \frac{d^2q}{(2\pi)^2} R(\boldsymbol{Q},\boldsymbol{q})\widehat{f}(\boldsymbol{q})\tilde{f}(\boldsymbol{Q}-\boldsymbol{q}) \tag{16}$$

and in the definition of the function

$$R(\boldsymbol{Q},\boldsymbol{q}) := (\hat{\boldsymbol{Q}}\times\boldsymbol{q})^2 \tag{17}$$

the vectors $\hat{\boldsymbol{Q}}$ and $\boldsymbol{q}$ are formally embedded in 3-dim. space for the sake of a compact and intuitive notation. Here it is important to keep in mind that (15) represents an effective field-theoretic Hamiltonian, in which a wave vector cutoff $|\boldsymbol{q}| < \Lambda$ for the modes $\widehat{f}(\boldsymbol{q})$ is implicit, and, of course, the numerical value of its parameters will also depend on the choice of Λ, which our notation reflects by introducing the subscript Λ in $\mathcal{H}_\Lambda, \kappa_\Lambda$ and K_Λ.

Hypothetically replacing $R(\boldsymbol{Q},\boldsymbol{q})$ by 1, $\widehat{\mathcal{F}}(\boldsymbol{Q})$ reduces to the Fourier transform of the squared OPD field $f^2(\boldsymbol{x})$. In this sense, we may say that $\widehat{\mathcal{F}}(\boldsymbol{q})$ has the structure of a "generalized square" [24]. Furthermore, the above effective Hamiltonian actually resembles a formal continuum limit of a discrete lattice model with lattice constant a, and in writing down (7) and (15), infrared and ultraviolet cutoffs $2\pi/ \leq |q_i| \leq \pi/a$ are implicitly understood. Thus, the above effective Hamiltonian for the flat phase of a crystalline model is accessible to our recently developed [25]

Fourier Monte Carlo (FMC) algorithm. In fact, the present situation is reminiscent of that of compressible spin models [26, 27], in which elimination of the phonons by Gaussian integration induces a long-range effective interaction for the spin degrees of freedom. For a detailed account on the nuts and bolts of FMC we refer to [28, 29, 24]. Here we content ourselves with the following brief description.

In applying the FMC algorithm to the present problem, universality authorizes us to consider the crystalline structure as a square lattice Γ of volume $V = La_0 \times La_0$ with $N_0 = L \times L$ sites and lattice constant a_0. In the present work, we use the the discrete Fourier conventions

$$f(\boldsymbol{x}) = \frac{1}{N_0} \sum_{\boldsymbol{q} \in \tilde{\Gamma}} \tilde{f}(\boldsymbol{q}) e^{i\boldsymbol{q}\boldsymbol{x}} \ , \qquad \tilde{f}(\boldsymbol{q}) = \sum_{\boldsymbol{x} \in \Gamma} f(\boldsymbol{x}) e^{-i\boldsymbol{q}\boldsymbol{x}} \tag{18}$$

for which the discrete Fourier amplitudes $\tilde{f}(\boldsymbol{q})$ are extensive quantities with the same physical dimension as the discretized field $f(\boldsymbol{x})$. These conventions, although asymmetric, are very convenient since, when combined with the rescaling

$$\widehat{f}(\boldsymbol{q}) \equiv a_0^2 \tilde{f}(\boldsymbol{q}) \tag{19}$$

they allow for easy translation of continuum formulae following the rules

$$\sum_{\boldsymbol{q} \in \widehat{\Gamma}} \leftrightarrow V \int_{\widehat{V}} \frac{d^2q}{(2\pi)^2}, \ \sum_{\boldsymbol{x}} \leftrightarrow \int \frac{d^2x}{a_0^2} \tag{20}$$

FMC employs these complex Fourier amplitudes $\tilde{f}(\boldsymbol{q})$ as basic MC variables. MC moves correspond to shifts

$$\tilde{f}(\boldsymbol{q}) \to \tilde{f}(\boldsymbol{q}) + \epsilon \delta_{\boldsymbol{q},\boldsymbol{q}_0} + \epsilon^* \delta_{\boldsymbol{q},-\boldsymbol{q}_0} \tag{21}$$

where ϵ is a random complex number with bounded modulus, and the wave vector $\boldsymbol{q}_0 \in \tilde{\Gamma}$ is chosen at random, but no reference to the direct lattice is made whatsoever. In the vast majority of situations encountered, this algorithm may be quite inefficient compared to real-space based ones, but for problems like coarse graining [25] and RG transformations [30, 31, 32] or, like in the present case, the computation of critical exponents [27], in which the subset of $\boldsymbol{q}$-vectors parameterizing the nonzero Fourier amplitudes can be confined to a narrow region bounded by wave vector cutoffs while the effect of the remaining modes is accounted for by the use of an effective Hamiltonian, it is ideally suited. This is even more so, if long-range interactions are involved [30, 33]. In the simulation of critical phenomena, it is essential to gather as much information as possible on the behavior of the system at "small" wave vectors, i.e. those around the critical wave vector ($\boldsymbol{q} = \boldsymbol{0}$ in the present case). Real space simulations necessarily take place in finite systems, of, say, linear size $L_0 a_0$, whose smallest accessible nonzero wave vector components are $2\pi/L_0 a_0$, but also have to deal with all other, increasingly unimportant modes up to the boundary of the Brillouin zone $|q_i| \leq \pi/a_0$ determined by the lattice constant a_0. However, if we are able to choose a wave vector cutoff $\Lambda \equiv \Lambda_0/b$, $b > 1$, and replace the original Hamiltonian by an effective one involving only modes with wave vectors inside Λ, then this corresponds to working with the original Hamiltonian at a system of lattice constant $a = ba_0$ and with $L = L_0/b$ unit cells in each direction, thus holding $N = N/b^2$ unit cells altogether. In turn this, implies that our FMC simulation effort with effective Hamiltonian and cutoff Λ resembles that of a direct lattice simulation with atomistic Hamiltonian on a system whose volume is b^2 times larger. In what follows we set a_0 to 1 and keep in mind that working at a cutoff Λ implies an effectively larger lattice constant $a \sim \pi/\Lambda$.

We now enter the discussion of the specific details of the present simulations. Since the effective Hamiltonians (1), (7) both involve spatial derivatives, we must first find a suitable discretization scheme. In a continuum Fourier transform, a partial derivative $\partial_j g(\boldsymbol{x})$ of a function $g(\boldsymbol{x})$ translates into multiplying its Fourier transform $\widehat{g}(\boldsymbol{q})$ by a factor $\widehat{\partial}(\boldsymbol{q}) = iq_j$, and taking the Laplacian gives a factor $\widehat{\Delta}(\boldsymbol{q}) = -\sum_{j=1}^{2} q_j^2 = -q^2$. On the lattice we may replace derivatives by Fourier transforms of nearest neighbor finite difference operators, which yields

$$\tilde{\partial}_j(\boldsymbol{q}) = \frac{i}{a}\sin aq_j,\ \tilde{\Delta}(\boldsymbol{q}) = -\frac{4}{a^2}\sum_{i=1}^{2}\sin^2\frac{aq_j}{2} \tag{22}$$

Of course, for $aq \to 0$, these operators asymptotically approach their continuum limits. However, working on a finite lattice with finite a, deviations from linearity in $\tilde{\partial}_j(\boldsymbol{q})$ and from cubic isotropy in $\tilde{\Delta}(\boldsymbol{q})$ become noticeable for large enough $\boldsymbol{q}$. In order to extract the exponent η from the $\boldsymbol{q}$-dependence of $\tilde{G}(\boldsymbol{q})$, it is essential to reduce these finite size effects, and in particular the accompanying cubic anisotropy. However, at the same time we would still like to maintaining overall periodicity in reciprocal space. For $\partial_j f(\boldsymbol{x})$, one may replace the above simple 2-point discretization by a four-point scheme (cf. [34], p. 15), which on Fourier transformation translates into

$$\tilde{\partial}_j(\boldsymbol{q}) = \frac{i}{a}\frac{(4-\cos aq_j)\sin aq_j}{3} \tag{23}$$

Let us take this approach one step further by considering a corresponding improved version of the lattice Laplacian $\tilde{\Delta}(\boldsymbol{q})$ derived from taking contributions from lattice neighbors beyond nearest neighborhood into account. Technically, in two dimensions this works as follows. One introduces polar coordinates $\boldsymbol{q} \to (q, \phi)$ and Taylor-expands an ansatz of type

$$\begin{aligned} -a^2\tilde{\Delta}(\boldsymbol{q}) \quad \equiv \quad & b + c(\cos aq_1 + \cos aq_2) + d[\cos a(q_1+q_2) + \cos a(q_1-q_2)] \\ & + e(\cos 2aq_1 + \cos 2aq_2) \\ & + f\Big[\cos a(q_1-2q_2) + \cos a(q_1+2q_2) + \cos a(2q_1-q_2) + \cos a(2q_1+q_2)\Big] + \ldots \end{aligned} \tag{24}$$

in q, successively choosing the coefficients b, c, d, e, f to eliminate low order ϕ-dependence, which by cubic symmetry must appear through terms proportional to $\cos(4\phi), \cos(8\phi), \ldots$ and unwanted low order powers of q except the leading q^2 one. Choosing $b = \frac{21}{5}, c = -\frac{26}{15}, d = -\frac{8}{15}, e = \frac{1}{30}$ and $f = \frac{1}{15}$, we obtain

$$-a^2\tilde{\Delta}(\boldsymbol{q}) = q^2 - \frac{q^6}{90} + O\left(q^8, \cos(4\phi), \cos(8\pi)\right) \tag{25}$$

such that cubic anisotropy is minimal for small enough cutoff Λ.

Since the notion of transverseness for a discretized system may not be well-defined independently of a chosen underlying discretization scheme, the safest way to discretize the membrane problem should be based on the original effective Hamiltonian (1) rather than (7). Nevertheless, even without resorting to the trick of splitting $f_{ij}(\boldsymbol{x})$ into transverse and longitudinal part, elimination of the IPD's by discrete Fourier transformation of all fields and Gaussian integration over the homogeneous and inhomogeneous contributions to $\tilde{\epsilon}_{ij}(\boldsymbol{q})$ is in principle straightforward, albeit tedious. The result is

$$\mathcal{H}[f] = \frac{\kappa_\Lambda}{2N}\sum_{\boldsymbol{q}\neq\boldsymbol{0}}\tilde{\Delta}(\boldsymbol{q})|\tilde{f}(\boldsymbol{q})|^2 + \frac{K_\Lambda}{2N}\sum_{\boldsymbol{Q}\neq\boldsymbol{0}}|\mathcal{F}(\boldsymbol{Q})|^2 \tag{26}$$

and

$$\mathcal{F}(\boldsymbol{Q}) = \frac{1}{2N} \sum_{\boldsymbol{q}\neq\boldsymbol{0},\boldsymbol{Q}} R(\boldsymbol{Q},\boldsymbol{p}) \tilde{f}(\boldsymbol{q}) \tilde{f}(\boldsymbol{Q}-\boldsymbol{q}) \tag{27}$$

The function $R(\boldsymbol{Q},\boldsymbol{p})$ is now defined as follows. We introduce the abbreviation $\tilde{\partial}(\boldsymbol{q}) \equiv i\tilde{\boldsymbol{q}}$ and form the 2×2 real-valued matrix

$$\mathcal{M}(\boldsymbol{Q}) = \frac{1}{\tilde{Q}_1^2 + \tilde{Q}_2^2} \begin{pmatrix} -\tilde{Q}_2^2 & \tilde{Q}_1\tilde{Q}_2 \\ \tilde{Q}_1\tilde{Q}_2 & -\tilde{Q}_1^2 \end{pmatrix} \tag{28}$$

Then it is not hard to see that in the long wavelength limit the real function

$$R(\boldsymbol{Q},\boldsymbol{q}) := \rho(\boldsymbol{q}|\boldsymbol{Q}|\boldsymbol{Q}-\boldsymbol{q}) \tag{29}$$

where

$$\rho(\boldsymbol{p}|\boldsymbol{Q}|\boldsymbol{q}) := \sum_{ij} \tilde{p}_i \mathcal{M}_{ij}(\boldsymbol{Q}) \tilde{q}_j \tag{30}$$

indeed reduces to the continuum version encountered in equation (17):

$$R(\boldsymbol{Q},\boldsymbol{q}) \to (\hat{\boldsymbol{Q}} \times \boldsymbol{q})^2 \quad \text{for} \quad \boldsymbol{Q},\boldsymbol{q} \to \boldsymbol{0} \tag{31}$$

This completes the description of our discretization scheme.

4. Optimization of FMC

In our present FMC simulations we monitored the set of squared moduli $|\tilde{f}(\boldsymbol{q})|^2$ for wave vectors $\boldsymbol{q}$ inside a suitably chosen cutoff Λ, together with their sum (33) and the total energy of the system. From the resulting separate time series of these MC data, which we also analyzed to ensure the complete equilibration of our simulations before MC measurements, we calculated estimates of the corresponding statistical error using the standard jackknife procedure [35, 36]. These estimates were cross-checked using the standard analysis of integrated autocorrelation times [37, 35] and the blocking method [38, 36] and we report nice numerical agreement of the different error estimates derived from these methods. An addition, we also introduce the following refinement to FMC. In the basic algorithm outlines by (21), the complex number ϵ is chosen at random within a circle of fixed radius r_ϵ in the complex plane. In the start-up phase of the simulation, one can incrementally adjust r_ϵ as to achieve a decent overall acceptance rate of FMC moves (usually somewhere between $30-60\%$). Still, as could have been anticipated from the well-known phenomenon of critical slowing down [36], one observes a dramatic growth of the integrated autocorrelation times $\tau_{\text{int}}(\boldsymbol{q})$ for $|\boldsymbol{q}| \to 0$, which in turn implies that, similar to the case of a real space algorithm based on non-collective moves, efficiency of plain FMC breaks down where we need it the most. Looking at the individual acceptance rates for moves of type (21) for different wave vectors $\boldsymbol{q}_0$, one realizes that this behavior results from the fact that for a uniform choice of r_ϵ, the acceptance rates for "small" $\boldsymbol{q}_0$-vectors are close to 100%, while they may fall well below 30% for large ones, which, however, make up the vast majority of $\boldsymbol{q}$-vectors, as the number of wave vectors of length q grows as q^{d-1} in d dimensions (cf. inset of figure 1). Since the equilibrium values of $|\tilde{f}(\boldsymbol{q}_0)|^2$ are dramatically larger for smaller than for larger wave vectors, this still implies that, since they all move on the same scale r_ϵ, the modes close to criticality make no headway in comparison to the noncritical ones. At this point, the following idea comes to rescue. In principle, (21) can be regarded as a different

type of MC move for each vector $\boldsymbol{q}_0$. Thus, without violating detailed balance, we can in principle pick a different value $r_\epsilon(\boldsymbol{q}_0)$ separately for each $\boldsymbol{q}_0$, offering the possibility to also tune the corresponding values $r_\epsilon(\boldsymbol{q}_0)$ separately. Of course, this tuning is not a trivial matter, since changing $r_\epsilon(\boldsymbol{q}_0)$ for one $\boldsymbol{q}_0$ will influence all other $r_\epsilon(\boldsymbol{q})$ in a possibly nonlinear way. Nevertheless, it is straightforward to implement a corresponding individual optimization for each $r_\epsilon(\boldsymbol{q}_0)$ during the start-up period of the simulation. And once this is done, we indeed observe an almost uniform common value of the integrated autocorrelation times $\tau_{\text{int}}(\boldsymbol{q})$ independent of the wave vector under consideration. In other words, on tuning $r_\epsilon(\boldsymbol{q}_0)$ individually, our FMC algorithm becomes free of critical slowing down! Actually, considering our previous work [29, 24], the underlying basic idea of this Optimized Fourier Monte Carlo (OFMC) algorithm is embarrassingly self-evident and should have come to mind much earlier. In fact, after completing this work we realized that even the authors of [21], who certainly were aware of our work, had come up with a similar idea. However, they had only considered occasional "wave vector moves" applied to a simple "pseudo-harmonic" model on top of a local MC move set defined in real space. Thus it is understandable that, despite of the resulting improvements that allowed them to correct the errors contained in their previous work [20], they obviously were not able to observe the dramatic reduction of autocorrelation times we report here.

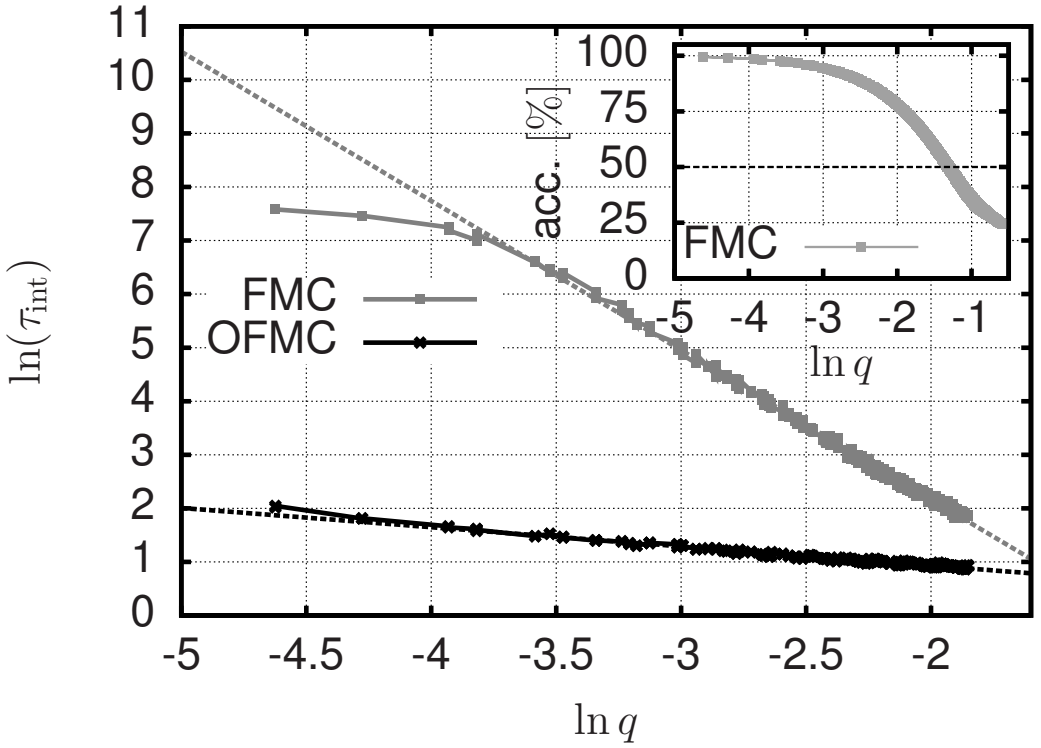

Figure 1. Main plot: Dramatic reduction of integrated autocorrelation times $\tau_{\text{int}}(\boldsymbol{q})$ for moduli $|\tilde{f}(\boldsymbol{q})|^2$ for our new OFMC algorithm in comparison to plain FMC for system size $L = 640$ and cutoff $\Lambda = \pi/8$. Deviations from linearity are due to the finite MC run time of 2^{20} MC steps (plain FMC) and finite tolerance $\pm 5\%$ for a 50% target acceptance (OFMC). Inset: q-dependent acceptance rates as measured for plain FMC.

5. Results

From the FMC point of view, the observables that suggest themselves naturally for the purpose of extracting η are, of course, $\tilde{G}(\boldsymbol{q}) = \langle|\tilde{f}(\boldsymbol{q})|^2\rangle$, and the mean square displacement $\langle(\Delta f)^2\rangle$. Let us first consider the latter.

5.1. Mean squared displacement $\langle(\Delta f)^2\rangle$

In continuum formalism $\langle(\Delta f)^2\rangle$ is calculated from $\widehat{G}(\boldsymbol{q})$ as

$$\langle(\Delta f)^2\rangle = G(\mathbf{0}) = \int \frac{d^2q}{(2\pi)^2}\widehat{G}(\boldsymbol{q}) \tag{32}$$

For $L \to \infty$, $\langle(\Delta f)^2\rangle$ diverges like $\langle(\Delta f)^2\rangle \sim L^{2\zeta}$, where ζ is known as the roughness exponent [8]. Explicitly calculating the integral (32) using the infrared cutoff $|q_i| \geq 2\pi/L$ and the scaling form (12) with (13), one easily finds the scaling relation $\zeta = 1 - \eta/2$. On our discrete lattice, the integral in (32) is, of course, replaced by the sum

$$(\Delta f)^2 \sim \sum_{\boldsymbol{q}} |\tilde{f}(\boldsymbol{q})|^2 \tag{33}$$

In contrast to $\tilde{G}(\boldsymbol{q})$, the observable $\langle(\Delta f)^2\rangle$ directly lends itself to a simple FSS approach. Trying to take possible sub-leading FSS corrections into account, we employ the ad hoc FSS ansatz

$$\langle(\Delta f)^2\rangle = \delta + \alpha L^{2-\eta}(1 + \beta/L + \gamma/L^2) \tag{34}$$

In providing proper data for an accurate FSS analysis, it is important to use a cubic cutoff geometry, since on a finite lattice the fraction of $\boldsymbol{q}$-vectors inside and outside of a fixed spherical cutoff generally does not scale with system size in a perfectly linear way. For the FSS analysis, we performed FMC simulations using the effective Hamiltonian (15) with renormalized parameters $\kappa_\Lambda = 0.1$, $K_\Lambda = 0.1$, in which a factor $(k_BT)^{-1}$ has been absorbed, and investigated a collection of systems with parameters

$$L = 32n,\ n = 1, 2, \ldots, 20, \quad \Lambda = \pi/8 \tag{35}$$

The above choice of parameters, which was used in the production runs, was fixed during the preparing test runs and was motivated by the heuristic principle to have an approximate balance of the harmonic and anharmonic contributions to the total average energy changes recorded during the simulation. For this choice, the largest considered system with $(L, \Lambda) = (640, 40)$ yields a value of $q_G/(2\pi/L) \approx 33$. In other words, we are able to evaluate a factor of ≈ 13 times more data describing the scaling region than those reported in [21]. Moreover, the statistical quality of these data is not affected by critical slowing down. And in fact, a standard least squares fit of (34) to our data works amazingly well (cf. figure 2). Numerically it results in the estimate

$$\eta = 0.795(10) \tag{36}$$

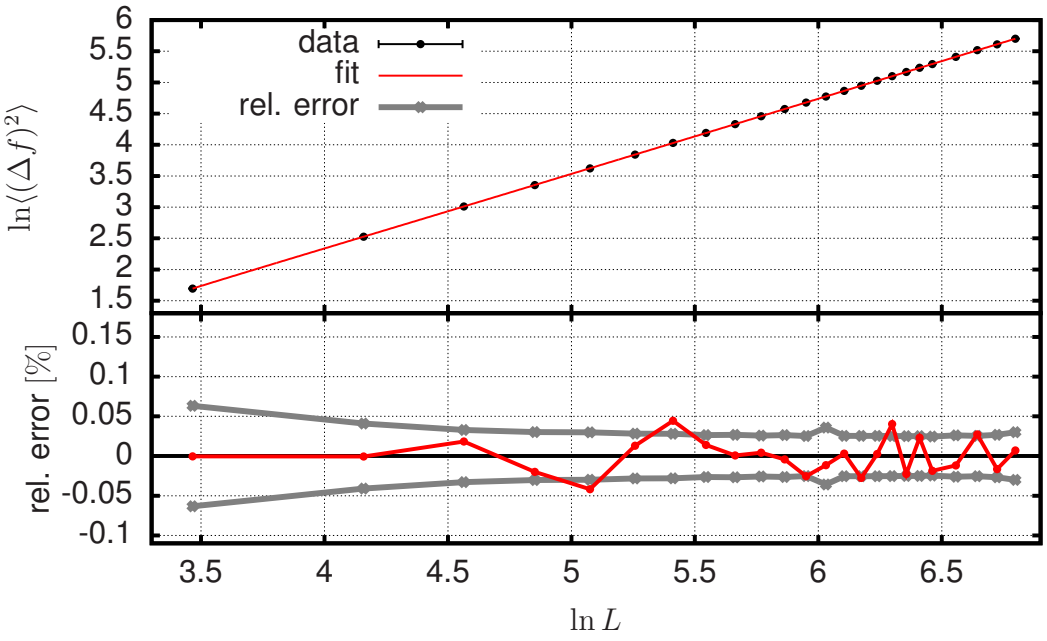

Figure 2. Top: fit of FSS ansatz (34) to simulation results for $\langle(\Delta f)^2\rangle$ obtained for the collection of systems (35). Error bars are smaller than symbol size. Bottom: Relative deviations of simulation data from the fit. Red lines are a guide to the eye. Gray lines indicate the relative statistical errors of the simulation data in percent.

5.2. Correlation function $\tilde{G}(\boldsymbol{q})$

As we now show, it is much harder to extract a reliable result for η from the critical scaling relation $\tilde{G}(\boldsymbol{q}) \sim k^{\eta-4}$. In view of (11-13), we actually should expect to see a crossover from MF behavior $\tilde{G}(\boldsymbol{q}) \sim q^{-4}$ for $q \gg q_G$ to critical scaling for $q \ll q_G$. However, it is difficult to judge the corresponding width of the crossover region. Thus, to reliably isolate η from a fit of the $\tilde{G}(\boldsymbol{q})$ data, an ansatz which allows for enough degrees of freedom to smoothly follow such a crossover behavior is required. In [13], Katsnelson considers a straightforward combination of the type

$$\tilde{G}^{-1}(\boldsymbol{q}) = \frac{\kappa_\Lambda q^4}{k_B T}\left[1 + \frac{1}{\alpha}\left(\frac{q_\Lambda}{q}\right)^\eta\right] \tag{37}$$

with a single free mixing parameter α (apart from the sought-after exponent η) that implicitly parameterizes the location of the crossover region in terms of a wave number $q_\Lambda = \sqrt{\frac{K_\Lambda}{\kappa_\Lambda}}$ introduced merely for dimensional reasons. Taking the logarithmic derivative of this expression, such an ansatz yields an effective exponent

$$\eta_{\text{eff}}(q) = \frac{\eta}{1 + \alpha\left(\frac{q}{q_\Lambda}\right)^\eta} \tag{38}$$

In [39], another type of crossover function is considered, which would translate into

$$\eta_{\text{eff}}(q) = \frac{\eta}{1 + \left(\frac{q}{q_\Lambda}\right)^\sigma} \tag{39}$$

in our present setting. Compared to Katsnelson's crossover function (38), this functional form rigidly fixes the location of the crossover on the q-axis, since it imposes $\alpha \equiv 1$. On the other hand, if we regard the parameter σ, which is fixed as $\sigma = (4-d)/2$ by the spatial dimension d in [39], as a free parameter in the present setting, it represents an additional degree of freedom that also allows to tune the width of the crossover region. A comparison of (38) and (39) thus suggests to introduce a more general crossover function with two free parameters α, σ, as

$$\eta_{\text{eff}}(q) \equiv \frac{\eta}{1+\alpha\left(\frac{q}{q_\Lambda}\right)^\sigma} \tag{40}$$

If we reintegrate this formula and nail down the unknown integration constant by comparing its asymptotics at $q \to \infty$ to the required MF behavior $\tilde{G}^{-1}(\boldsymbol{q}) \sim q^4$, we obtain

$$\tilde{G}^{-1}(\boldsymbol{q}) = \frac{\kappa_\Lambda q^4}{k_B T} \cdot \left[1 + \frac{1}{\alpha}\left(\frac{q_\Lambda}{q}\right)^\sigma\right]^{\eta/\sigma} \tag{41}$$

which is the general fitting function with parameters η, σ and α we used to describe our data.

As a further refinement, we made an effort to correct for residual traces of the underlying discretization (i.e. spurious higher powers of q and cubic anisotropy effects implicitly caused by the replacements $\boldsymbol{q} \to \tilde{\boldsymbol{q}}$ and $q^2 \to -\tilde{\Delta}(\boldsymbol{q})$). In polar coordinates $\boldsymbol{q} \to (q, \phi)$, such corrections should be of the general form

$$|\boldsymbol{q}| \to |\boldsymbol{q}|_{\text{corr}} = q + (a_3 + b_3 \cos 4\phi) q^3 + (a_5 + b_5 \cos 4\phi + c_5 \cos 8\phi) q^5 + \ldots \tag{42}$$

In fitting (41) to the $\tilde{G}(\boldsymbol{k})$ data this replacement was made, treating a_3, b_3, a_5, b_5 and c_5 as additional fit parameters. However, this correction turned out to be of minor importance. Another concern was that since the number of $\boldsymbol{q}$-vectors of length q in two dimensions grows linearly with q, the data points in the scaling region might be underrepresented in a straightforward least squares fit. Thus, fits were performed using a minimization procedure for a sum of squared differences, weighted not only by the inverse variances of the data points, but in addition also by $q^{-\omega}$ for values $\omega = 0.0$, 0.5 and 1.0. To calculate proper statistical error bars for this hand-made weighted fit procedure, we employed a standard bootstrap approach [40] using 100 bootstrap samples. However, it turned out that for all values of ω the results were statistically compatible with each other, the smallest error resulting for $\omega = 0$.

Figure 3 shows the typical results of such a fit obtained for a large system of linear size $L = 1800$ and cutoff $\Lambda = \pi/15$ (corresponding, as explained above, to a real space system of linear size $L_0 = 27000$) from a parallel version of our FMC code which will be described elsewhere. At first glance, the fit looks quite acceptable, producing a value of $\eta = 0.751 \pm 0.017$. However, monitoring the relative deviations of individual data from the fit as compared to their relative statistical errors, we notice that while most of the deviations remain in the range of the statistical noise of the data, for the smallest $\boldsymbol{q}$-vectors $(1,0) \cdot 2\pi/L$ and $(0,1) \cdot 2\pi/L$ that we can study on the cubic lattice the deviation exceed 10%. Following next in size are the vectors $(1,1) \cdot 2\pi/L$ and $(1,-1) \cdot 2\pi/L$, who also show a noticeable deviation, albeit much smaller and opposite in its tendency. This behavior is in violent conflict with the supposed scaling behavior, but our error bars are much too small to put the blame on statistical inaccuracies. Clearly, a similar behavior will also be seen for any other reasonable choice of fitting function.

Let m, n denote two arbitrary integers. In the following we will denote the set of all wave vectors $(m,n) \cdot 2\pi/L$ together with all vectors which are equivalent to these modulo cubic symmetry as as $(m,n)_c$ and refer to this set as a (cubic) symmetric direction. A separate analysis of the deviations in various such symmetric directions (cf. figure 4) reveals a certain systematic behavior detectable on top of the statistical noise for vectors along $(1,0)_c$ and $(1,1)_c$,

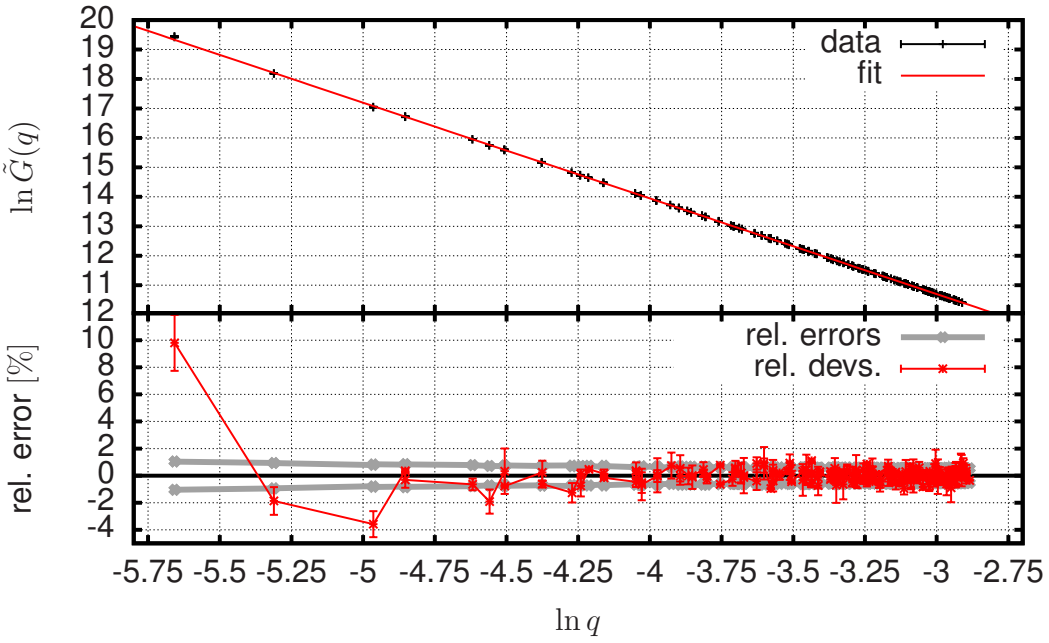

Figure 3. Top: fit of crossover ansatz (41) to simulation results for $\tilde{G}(\boldsymbol{q})$ at linear system size $L = 1800$ and cutoff $\Lambda = \pi/15$. Error bars are smaller than symbol size. Bottom: Relative deviations of simulation data from the fit. Red lines are a guide to the eye. Gray lines indicate the relative statistical errors of the simulation data in percent.

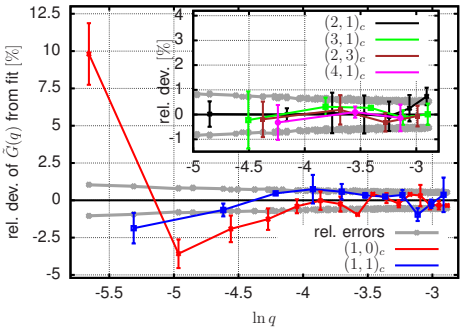

Figure 4. Separate comparison of relative deviations of simulation data for $\tilde{G}(\boldsymbol{q})$ for wave vectors $\boldsymbol{q}$ along various symmetric directions as indicated. Lines are a guide to the eye. Gray lines indicate the relative statistical errors of the simulation data in percent. Main plot: symmetric directions of type $(1,0)_c, (1,1)_c$. Inset: various other directions.

which decreases rapidly with the length of the corresponding wave vector, while the remaining modes reveal no such behavior within statistical errors. Initially suspecting a bug in our code, we introduced a number of modifications to our original program to investigate this phenomenon further. To eliminate possible anisotropy effects originating form a cubic cutoff geometry, we replaced the cubic cutoff $|q_i| \leq \Lambda$ by a spherical one with $|\boldsymbol{q}| \leq \Lambda$. We also performed additional simulations using modified discretization schemes for $\tilde{\partial}(\boldsymbol{q})$ and $\tilde{\Delta}(\boldsymbol{q})$. Since we recall infrequent reports on spurious oscillations arising from the use of sharp cutoffs in the literature on the exact renormalization group [41], we even tried to replace our sharp cutoff by a soft one, i.e. we introduced a modification of the dispersion function $\tilde{\Delta}(\boldsymbol{q})$, which rises smoothly near the boundary of the cutoff and finally diverges beyond Λ. None of these modifications had a noticeable effect on the observed special behavior of the $(1,0)_c$ and $(1,1)_c$ modes. However, switching off anharmonicity by hand by putting $K = 0$ immediately eliminates the problem, and so does the brute force modification $R(\boldsymbol{Q}, \boldsymbol{q}) \equiv 1$. Finally, we chose to investigate the following

toy model. Consider two wave vectors $\boldsymbol{k}, \boldsymbol{p}$, and let $\boldsymbol{Q} = \boldsymbol{k} + \boldsymbol{p}$. Taking the angular average of the continuum limit formula (17)

$$R(\boldsymbol{k}+\boldsymbol{p}, \boldsymbol{k}) = ((\widehat{\boldsymbol{k}+\boldsymbol{p}}) \times \boldsymbol{p})^2 = \frac{k^2 p^2 + (\boldsymbol{k}\boldsymbol{p})^2}{(\boldsymbol{k}+\boldsymbol{p})^2} \tag{43}$$

yields

$$\langle R(\boldsymbol{k}+\boldsymbol{p}, \boldsymbol{k})\rangle_\phi = \frac{k^2 + p^2 + (p+q)|p+q|}{4} \tag{44}$$

Plugging this into our algorithm, we again observe that any possible residual pathological deviations of the $(1,0)_c$ and $(1,1)_c$ modes are dissolved in the statistical noise of the data. Although these ad hoc replacements of $R(\boldsymbol{Q}, \boldsymbol{q})$ are, of course, physically unacceptable, they nevertheless demonstrate that the behavior reported above is very unlikely caused by a mere bug in our code, but seems to be related to the angle-dependent structure between $\boldsymbol{k}$ and $\boldsymbol{p}$ of encoded in (43) in combination with the finite size of the system. We currently believe that it represents an, albeit completely unexpected and somewhat exotic, finite size effect resulting from the interplay of the effective Hamiltonian (26) with the topology of underlying set of admissible wave vectors, which induces a kind of "surface effect in reciprocal space". Indeed, the subset of wave vectors of the Brillouin zone taking part in the simulation is bounded by the cutoff Λ for large wave vectors. In a transition with critical wave vector $\boldsymbol{q}_c = \boldsymbol{0}$, the modes with large $\boldsymbol{q}$-vectors just below the cutoff Λ are the least critical and are not expected to contribute significantly to the critical asymptotics. However, in the special care of the current membrane problem, the Brillouin zone of a finite membrane represents a lattice, in which a hole is pinched at its center $\boldsymbol{q} = \boldsymbol{0}$, inducing an additional "boundary" besides the one defined by Λ, and the resulting cubic anisotropy is felt by the small wave vector modes in its neighborhood. Intuitively, the effect of this hole at the center of the Brillouin zone may be viewed as a breaking of anharmonic "reciprocal space bonds" that are mediated by the strongly direction-dependent coupling (43). And in contrast to the large wave vector cutoff, modes with small q do fluctuate violently, while (43) reveals that the couplings to all other modes are bounded by q and thus small. For the smallest admissible wave vectors $(2\pi/L, 0)$ and $(0, 2\pi/L)$, we may thus expect a certain deviatoric tendency of $\tilde{G}(\boldsymbol{q})$ towards MF behavior (and thus "up"), which is indeed identified in the data as the large positive deviation of $\tilde{G}(\boldsymbol{q})$ at this wave vector in figure 4. For larger vectors, however, we find it difficult to predict even the qualitative behavior of the resulting anisotropy.

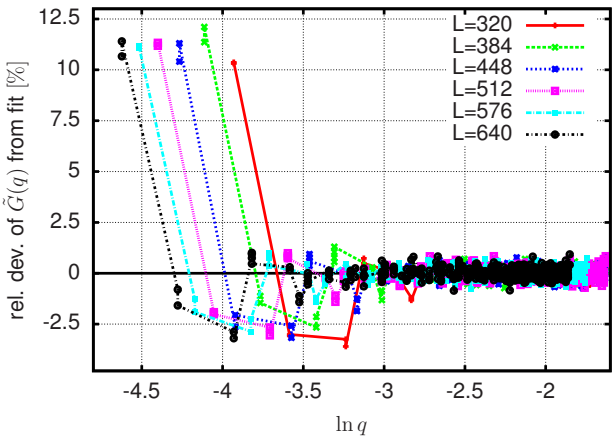

Figure 5. Comparison of relative deviations of simulation data for $\tilde{G}(\boldsymbol{q})$ as observed for the collection of systems (35).

Based on the hypothesis that what we see at small wave vectors is a finite size effect, we decided to monitor the corresponding systematic trends observed with growing system size. As figure 5 demonstrates, the pathological effects observed in the deviations of the $\tilde{G}(\boldsymbol{k})$ data from the collective trends found in a least squares fit of all modes are indeed qualitatively completely similar for all considered system sizes, but for growing system size L are confined to a successively shrinking region around $\boldsymbol{q} = \boldsymbol{0}$. It is thus reasonable to expect that these irregularities may indeed asymptotically disappear in the thermodynamic limit.

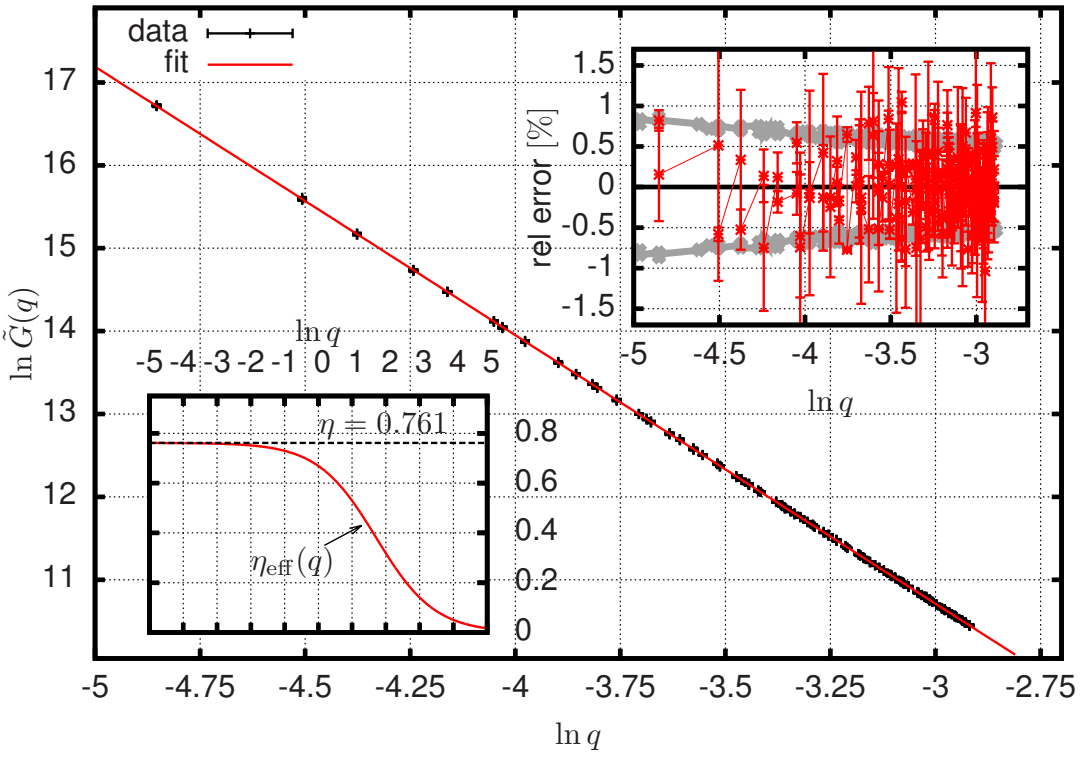

Figure 6. Main plot: fit of crossover ansatz (41) to simulation results for $\tilde{G}(\boldsymbol{q})$ with all contributions for $\boldsymbol{q}$-vectors of type $(1,0)_c$ and $(1,1)_c$ omitted. Error bars are smaller than symbol size. Right upper inset: relative deviations of simulation data from the fit. Red lines are a guide to the eye. Gray lines indicate the relative statistical errors of the simulation data in percent. Left lower inset: crossover function (40) as determined by the fit.

As a finite size effect, the presence of the above described deviations should be properly covered by our FSS ansatz (34). In addition, note from figure 4 that the tendencies observed in the small wave vector deviations along $(1,0)_c$ and $(1,1)_c$ are different, and therefore tend to at least partially compensate themselves in the total sum (33). Thus, we are still confident that the estimate (36) is correct.

To be able to squeeze out a reasonable numerical estimate from $\tilde{G}(\boldsymbol{q})$ for comparison, we decided to omit the most deviatoric $(1,0)_c$ and $(1,1)_c$ data in performing our fits. As figure 6 shows, the quality of the resulting fit is excellent, producing the result

$$\eta = 0.761 \pm 0.008 \tag{45}$$

However, it is not straightforward to combine this estimate with our previous one. On the one hand, the difficulties encountered in deriving (45) may be the source of a systematic error

superimposed on the observed statistical uncertainties. On the other hand, our guess (40) for the true crossover function $\eta_{\rm eff}(k)$ may still be less than perfect, introducing an additional systematic error in the result. Last but not least, a small conventional finite size effect may still remain. Reviewing these arguments we cannot help falling back on our previous FSS result (36), which is not plagued by these difficulties.

6. Conclusion

In summary, we have presented a thorough discussion of our OFMC approach to calculating the critical exponent η governing the long wavelength scaling of elastic deformations of crystalline membranes in the flat phase. The great efficiency and excellent statistical accuracy of OFMC is basically due to two reasons. On the one hand, by working with the Fourier amplitudes of deformations as the basic MC variables and using an effective Hamiltonian at a wave vector cutoff, we manage to project out all uninteresting microscopic details and to focus only on the long wavelength degrees of freedom that determine the universal critical behavior. On the other hand, we are using the collective MC move set (21), for which we manage to overcome critical slowing down by tuning the MC acceptance rates separately for each $\boldsymbol{q}$ vector, which yields a huge effective speedup of our simulations.

In future work, we plan to investigate the behavior of crystalline membranes close to a substrate and/or under uniaxial tension. We also expect a similar approach to work for hexatic membranes [12]. However, the OFMC approach is, of course, not limited to membranes. Further applications to e.g. compressible spin systems and other long-range lattice spin models are under way.

Note added in proof. A short account on the results presented above has now been published in [42].

Acknowledgments

Major parts of our computations were performed on the Vienna Scientific Cluster (VSC2). We are grateful for support by the Austrian Science Fund (FWF) Project P22087-N16 and would like to thank K. Binder, C. Dellago, G. Kahl, M. Katsnelson and U. Pedersen for valuable discussions.

References

[1] Nelson D, Piran T and Weinberg S (eds) 2004 *Statistical Mechanics of Membranes and Surfaces, Second Edition* (Singapore: World Scientific)
[2] Leibler S 2004 *Statistical Mechanics of Membranes and Surfaces, Second Edition* ed Nelson D et al (Singapore: World Scientific) chapter 3 pp 49–101
[3] De Gennes P and Taupin C 1982 *J. Phys. Chem.* **86** 2294
[4] Mermin N and Wagner H 1966 *Phys. Rev. Lett.* **17** 1133
[5] Peliti L and Leibler S 1985 *Phys. Rev. Lett.* **54**(15) 1690–1693
[6] Novoselov K S, Jiang D, Schedin F, Booth T J, Khotkevich V V, Morozov S V and Geim A K 2005 *Proceedings of the National Academy of Sciences of the United States of America* **102** 10451–10453
[7] Pisana S, Lazzeri M, Casiraghi C, Novoselov K, Geim A, Ferrari A and Mauri F 2007 *Nature Mat.* **6** 198
[8] Bowick M J 2004 *Statistical Mechanics of Membranes and Surfaces, Second Edition* ed Nelson D et al (Singapore: World Scientific) chapter 11 p 323
[9] Chaikin P M and Lubensky T 1995 *Principles of Condensed Matter Physics* (Cambridge, UK: Cambridge University Press)
[10] Bowick M and Travesset A 2001 *Phys. Rept.* **344** 255
[11] Nelson D and Peliti L 1987 *J. Phys. (Paris)* **48** 1085
[12] Nelson D 2004 *Statistical Mechanics of Membranes and Surfaces, Second Edition* ed Nelson et al (Singapore: World Scientific) chapter 6 p 131
[13] Katsnelson M I 2012 *Graphene: Carbon in Two Dimensions* (Cambridge, UK: Cambridge University Press)
[14] Gompper G and Kroll D M 2004 *Statistical Mechanics of Membranes and Surfaces, Second Edition* ed Nelson D et al (Singapore: World Scientific) chapter 12 pp 359–426

[15] Le Doussal P and Radzihovsky L 1992 *Phys. Rev. Lett.* **69** 1209
[16] Aronovitz J A and Lubensky T 1988 *Phys. Rev. Lett.* **60** 2634
[17] David F and Guitter E 1988 *Europhys. Lett.* **5** 709
[18] Kownacki J P and Mouhanna D 2009 *Phys. Rev. E* **79**(4) 040101
[19] Bowick M J, Catterall S M, Falcioni M, Thorleifsson G and Anagnostopoulos K N 1996 *J. Phys. I France* **6** 1321
[20] Fasolino A, Los J and Katsnelson M I 2007 *Nature Materials* **6** 858
[21] Los J H, Katsnelson M I, Yazyev O V, Zakharchenko K V and Fasolino A 2009 *Phys. Rev. B* **80**(12) 121405(R)
[22] Zakharchenko K V, Los J H, Katsnelson M I and Fasolino A 2010 *Phys. Rev. B* **81**(23) 235439
[23] Zakharchenko K V, Roldán R, Fasolino A and Katsnelson M I 2010 *Phys. Rev. B* **82**(12) 125435
[24] Tröster A and Dellago C 2010, Physics Procedia **6**, pp 106–116
[25] Tröster A 2007 *Phys. Rev. B* **76** 012402
[26] Bergman D and Halperin B 1976 *Phys. Rev. B* **13** 2145
[27] Tröster A 2008 *Phys. Rev. Lett.* **100** 140602
[28] Tröster A and Dellago C 2007 *Ferroelectrics* **354** 225
[29] Tröster A 2008 *Comput. Phys. Comm.* **179** 30
[30] Tröster A 2009 *Phys. Rev. E* **79** 036707
[31] Tröster A 2010 *Phys. Rev. B* **81** 125135
[32] Tröster A 2011 *Computer Physics Communications* **182** 1837–1841
[33] Tröster A 2010 *Phys. Rev. B* **81** 012406
[34] Moin P 2010 *Fundamentals of Engineering Numerical Analysis* (Cambridge, UK: Cambridge University Press)
[35] Berg B A 2004 *Markov Chain Monte Carlo Simulations and Their Statistical Analysis* (Singapore: World Scientific)
[36] Amit D and Martin-Mayor V 2005 *Field Theory, the Renormalization Group, and Critical Phenomena: Graphs to Computers (3rd Edition)* (Singapore: World Scientific)
[37] Binder K and Heermann D W 2010 *Monte Carlo Simulations in Statistical Physics* 5th ed Graduate Texts in Physics (Berlin: Springer)
[38] Flyvbjerg H and Petersen H G 1989 *The Journal of Chemical Physics* **91** 461–466
[39] Luijten E and Binder K 1998 *Phys. Rev. E* **58** R4060
[40] Efron B and Tibshirani R 1994 *An Introduction to the Bootstrap* (Boca Raton: Chapman and Hall)
[41] Morris T R and Tighe J F 1999 *Journal of High Energy Physics* **1999** 007
[42] Tröster A 2013 *Phys. Rev. B* **87** 104112